K.M. Hanson (ed.), *Proc. SPIE's International Symposium Medical Imaging: Image Processing, San Diego, CA, USA,* Vol. 3338, pp. 28-38. SPIE, 1998.

Refined Localization of Three-Dimensional Anatomical Point Landmarks Using Multi-Step Differential Approaches

Sönke Frantz, Karl Rohr, H. Siegfried Stiehl

Arbeitsbereich Kognitive Systeme, Fachbereich Informatik,
Universität Hamburg, D-22527 Hamburg, Germany
E-Mail: frantz@informatik.uni-hamburg.de

ABSTRACT

In this contribution, we are concerned with the detection and refined localization of 3D point landmarks. We propose multi-step differential procedures which are generalizations of an existing two-step procedure for subpixel localization of 2D point landmarks. This two-step procedure combines landmark detection by applying a differential operator with refined localization through a differential edge intersection approach. In this paper, we theoretically analyze the localization performance of this procedure for analytical models of a Gaussian blurred L-corner as well as a Gaussian blurred ellipse. By varying the model parameters differently tapered and curved structures are represented. The results motivate the use of an analogous procedure for 3D point landmark localization. We generalize the edge intersection approach to 3D and, by combining it with 3D differential operators for landmark detection, we propose three multi-step procedures for subvoxel localization of 3D point landmarks. The multi-step procedures are experimentally tested for 3D synthetic images and 3D MR images of the human head. We show that the multi-step procedures significantly improve the localization accuracy in comparison to applying a 3D detection operator alone.

Keywords: 3D anatomical point landmarks, Human brain, 3D differential operators, 3D edge intersection approach, Point landmark localization, Point-based image registration

1. INTRODUCTION

Point-based registration of images generally depends on the extraction of suitable point landmarks. In particular, the registration of 3D medical images for applications in neurosurgery requires high-precision landmark localization. Potential landmarks of the human head are salient tips which can be found, for instance, on the ventricular system, on the skull base, as well as on other anatomical structures. Usually, such 3D landmarks are manually selected—a task which is difficult, time-consuming, and often lacks accuracy. As an alternative, we here consider a semi-automatic procedure for landmark selection which has the advantage that the user can interactively control the results. First, an approximate position of a specific landmark is manually determined. Second, to extract potential landmark candidates, a computational approach is applied within a region-of-interest (ROI) around the approximate position. Third, the user selects the most promising candidate. The computational approach has to reliably and robustly detect as well as to accurately localize prominent points. Recently, 3D differential operators have been introduced which, however, are only designed for the detection of point landmarks.[1–4] Since reliable and robust landmark detection generally requires large-sized operators, the accuracy of the detected points often is not satisfactory and additional steps are necessary to obtain better position estimates.

In this contribution, we are concerned with the detection and refined localization of 3D point landmarks. We propose multi-step differential procedures for subvoxel landmark localization. The multi-step procedures are based on a two-step procedure for subpixel localization of 2D point landmarks.[5] This procedure combines landmark detection by applying a differential operator with refined localization through a differential edge intersection approach. In this paper, we first investigate the localization performance of the two-step procedure for 2D analytical models of a Gaussian blurred L-corner as well as a Gaussian blurred ellipse. By varying the model parameters differently tapered and curved structures are represented. The results of this study motivate the use of an analogous procedure for 3D point landmark localization. Then, we generalize the edge intersection approach to 3D and, by combining it with existing 3D differential operators for landmark detection, we propose multi-step differential procedures for subvoxel landmark localization. The multi-step procedures are experimentally tested for 3D synthetic images and 3D MR images of the human head.

2. TWO-STEP PROCEDURE FOR 2D POINT LANDMARK LOCALIZATION

Förstner and Gülch[5] proposed a procedure for 2D point landmark localization which comprises two steps. First, landmark candidates are detected by applying a differential operator. Second, the positions are refined through a differential edge intersection approach. The procedure was applied to 2D images of polyhedral objects as well as to 2D aerial images. Recently, the differential operator used in the two-step procedure has been evaluated w.r.t. its detection capabilities on 2D tomographic images of the human brain.[6] In the following, we summarize the two-step procedure.

Landmark detection The used differential operator[7,8] exploits the matrix

$$\mathbf{N} = \begin{pmatrix} \sum_i g_{x_i}^2 & \sum_i g_{x_i} g_{y_i} \\ \sum_i g_{x_i} g_{y_i} & \sum_i g_{y_i}^2 \end{pmatrix}.$$

The subscripts x and y of the image function $g(x,y)$ stand for the partial derivatives in the respective spatial direction and the sum index i denotes the spatial location. The operator reads

$$F(\mathbf{x}) = \frac{det(\mathbf{N})}{tr(\mathbf{N})}, \tag{1}$$

where $det(\cdot)$ denotes the determinant and $tr(\cdot)$ denotes the trace of a matrix. Each point $\mathbf{x} = (x,y)$ in the image is being assigned the measure in (1), where the matrix $\mathbf{N}$ is usually computed in a symmetric observation window of certain size around $\mathbf{x}$. Point landmarks are detected by searching for local maxima of the operator responses.

Refined localization Suppose an L-corner has been detected and the observation window around the detected position captures sufficient edge information of the structure. For simplicity, a local coordinate system with the detected point as origin is chosen. At each edge point in the observation window a tangent is defined to locally approximate its corresponding edge. For this, the image gradients are taken as normals to the tangents. The tangents are represented in the Hessian form. For example, for a point $\mathbf{x}_i$ with gradient ∇g_i the Hessian form reads $< \nabla g_i, \mathbf{x} > = < \nabla g_i, \mathbf{x}_i >$, where $< \cdot, \cdot >$ denotes the inner product. Rewriting this equation to $\varepsilon_i(\mathbf{x}) = < \nabla g_i, \mathbf{x} - \mathbf{x}_i >$ yields the perpendicular distance from $\mathbf{x}$ to the tangent at $\mathbf{x}_i$. Note that the distance is implicitly multiplied with the gradient magnitude since ∇g_i generally is not a unit vector. An estimate for the position of the tip can be obtained through intersection of all tangents using the least-squares-method, that is, through minimization of the residual error function

$$\mathrm{E}(\mathbf{x}) = \sum_i \varepsilon_i(\mathbf{x})^2. \tag{2}$$

So far, solely edge points have been considered. However, due to implicitly weighting the residual errors with the gradient magnitude, it is possible to abolish this restriction and to include in the sum in (2) all points within the observation window. Points in rather homogeneous regions with low gradient magnitude should hardly contribute to the sum anyway. On the other hand, edge points with generally high gradient magnitude should actually force a small distance from the position estimate to their corresponding tangent. Finally, the condition $\nabla \mathrm{E}(\mathbf{x}) = \mathbf{0}$ yields a system of normal equations

$$\mathbf{N}\mathbf{x}^* = \mathbf{y}, \tag{3}$$

where $\mathbf{x}^*$ denotes the estimated position of the tip and

$$\mathbf{y} = \begin{pmatrix} \sum_i g_{x_i}^2 x_i + \sum_i g_{x_i} g_{y_i} y_i \\ \sum_i g_{x_i} g_{y_i} x_i + \sum_i g_{y_i}^2 y_i . \end{pmatrix}.$$

3. LOCALIZATION PERFORMANCE FOR 2D ANALYTICAL MODELS

It is known that for an L-corner the detection operator in (1) yields systematic localization errors w.r.t. the correct corner position.[9] The error generally depends on the image blur, the aperture angle of the L-corner, and the operator size. Hence, in general, additional steps are necessary to obtain better position estimates. In the following, we analyze the localization performance of the two-step procedure of Förstner and Gülch[5] in comparison to applying the detection operator alone. We investigate analytical models of a Gaussian blurred L-corner[10] as well as a Gaussian blurred ellipse (see Figs. 1a and 2a).

The standard deviation of the Gaussian blur function has been set to $\sigma = 1$. The analytically calculated partial derivatives of the model functions have been used for the computation of the elements of the matrix $\mathbf{N}$ and the vector $\mathbf{y}$ in (3). We have used the approximation

$$\mathbf{N} \approx \nabla g(\mathbf{x}) \nabla g(\mathbf{x})^T + c\mathbf{H}_g(\mathbf{x})^2$$

to compute the operator responses $F(\mathbf{x})$ in (1). The parameter c is a measure for the size of the observation window of the detection operator and $\mathbf{H}_g(\mathbf{x})$ denotes the Hessian matrix of the image function. We have used $c = 2/3$ which stands for a window width of $3pix$, where pix denotes spatial unity. The search for maxima of the response of the detection operator has been restricted to the symmetric axis of the models, that is, the x-axis.

L-corner In Fig. 1a, an L-corner with the aperture angle β is shown. In Fig. 1b, the distances e from the localized positions to the correct corner position are depicted in dependence on β. The solid line results from the detection operator alone and the dashed line results from the two-step procedure using the edge intersection approach. The size of the observation window for the edge intersection approach has been the same as that for the detection operator, that is, 3×3 pixels. The localization error for the detection operator alone heavily depends on the aperture angle β. The localization error is very small for values near $\beta = 180°$ and high for small values of β. The position estimates resulting from the edge intersection approach are significantly more accurate. In fact, the additional second step improves the accuracy for about $1pix$ for a large range of values of β. Moreover, we can obtain even better position estimates if we further enlarge the observation window for the edge intersection approach and thus take more edge information into account. The result for a size of 15×15 pixels is shown in Fig. 1c. It can be seen that the localization error is nearly zero.

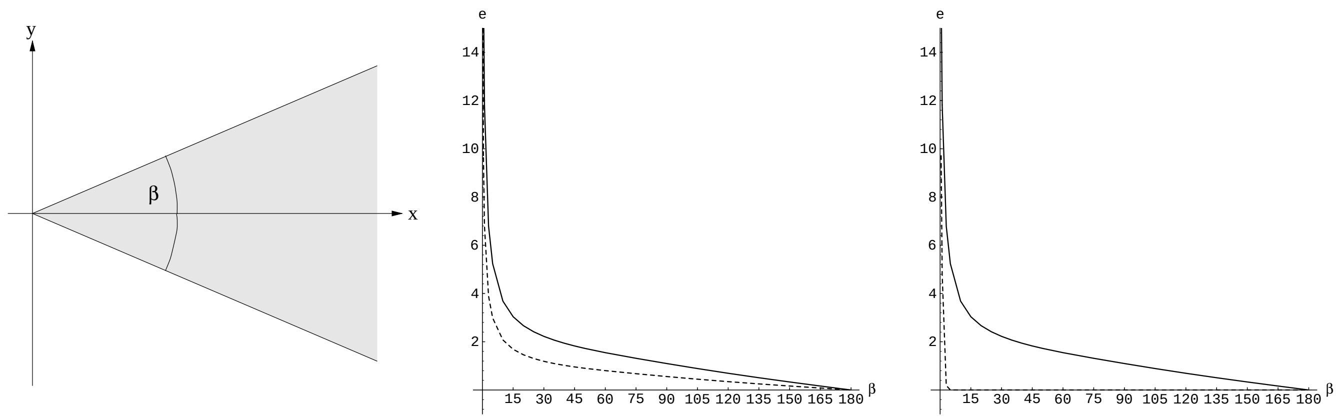

a. b. c.

Figure 1a. L-corner with aperture angle β. **b and c.** Localization accuracy for a Gaussian blurred L-corner with $\sigma = 1$. The distances e from the localized positions to the correct corner position (ordinate) are depicted in dependence on the aperture angle β (abscissa). The solid line results from the detection operator alone and the dashed line results from the two-step procedure. Observation windows of sizes 3×3 pixels (b) and 15×15 pixels (c) have been used (see text).

Ellipse In Fig. 2a, an ellipse with half-axes lengths a and b is shown. The considered point landmark is the tip at $(a, 0)$. We have investigated ellipses with different shapes. For this, we have varied the ratio a/b. For example, a large value gives a more tapered shape and a value near 1 gives a more rounded shape. We have varied a starting with $a = 6$ and have permanently set $b = 4$. In Fig. 2b, the distances e from the localized positions to the position of the tip are depicted in dependence on the ratio a/b. The localization error resulting from the detection operator alone amounts on average to a bit more than $1pix$. Again, the second step of the procedure significantly improves the localization accuracy. However, the localization error increases for the edge intersection approach if we further enlarge the observation window. This is because the ellipse deviates from the assumed polygonal model and this deviation increases if we enlarge the observation window. Nevertheless, in Fig. 2c it is shown that even for an observation window of size 7×7 pixels the position estimates resulting from the edge intersection approach are more accurate than those resulting from the detection operator alone.

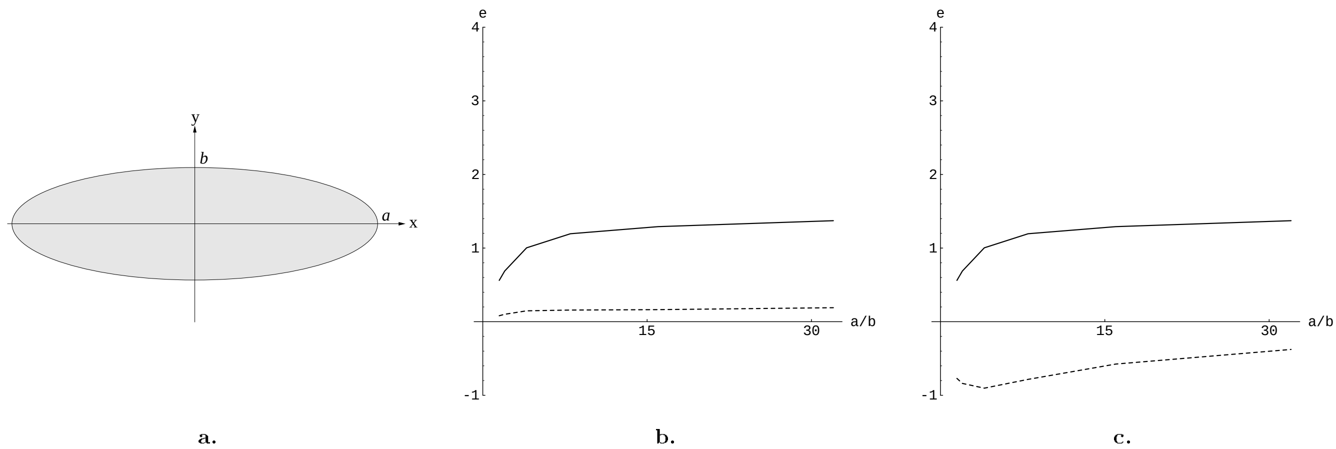

Figure 2a. Ellipse with half-axes lengths a and b. **b and c.** Localization accuracy for a Gaussian blurred ellipse with $\sigma = 1$. The distances e from the localized positions to the position of the tip at $(a, 0)$ (ordinate) are depicted in dependence on the ratio a/b (abscissa), where we have varied a starting with $a = 6$ and have permanently set $b = 4$. The solid line results from the detection operator alone and the dashed line results from the two-step procedure. Observation windows of sizes 3×3 pixels (b) and 7×7 pixels (c) have been used (see text).

Our investigation has demonstrated the superior localization capabilities of the two-step procedure in comparison to applying a detection operator alone and hence motivates the use of an analogous procedure for 3D point landmark localization.

4. EXTENSION OF THE EDGE INTERSECTION APPROACH TO 3D

In this section, we generalize the edge intersection approach[5] to 3D. A 3D extension of an L-corner is a tetrahedron which is shown in Fig. 3a. Suppose we have detected the tip of a tetrahedron. Assume we have placed there an observation window capturing sufficient information of the structure. The position of the tip is the intersection point of three planar surfaces which correspond to 3D edges. Analogously to the 2D case, we locally approximate the surfaces through tangent planes. The image gradients are taken as normals to the tangent planes. The Hessian form of the tangent plane at a point $\mathbf{x}_i$ reads $< \nabla g_i, \mathbf{x} > = < \nabla g_i, \mathbf{x}_i >$. The position of the tip can be estimated through intersection of all tangent planes using the least-squares-method, that is, through minimization of a residual error function which formally agrees with that in (2) of the 2D edge intersection approach. As in the 2D case, we obtain a system of normal equations

$$\mathbf{N}\mathbf{x}^* = \mathbf{y}, \tag{4}$$

where $\mathbf{x}^*$ denotes the estimated position of the tip and where

$$\mathbf{N} = \begin{pmatrix} \sum_i g_{x_i}^2 & \sum_i g_{x_i} g_{y_i} & \sum_i g_{x_i} g_{z_i} \\ \sum_i g_{x_i} g_{y_i} & \sum_i g_{y_i}^2 & \sum_i g_{y_i} g_{z_i} \\ \sum_i g_{x_i} g_{z_i} & \sum_i g_{y_i} g_{z_i} & \sum_i g_{z_i}^2 \end{pmatrix}$$

and

$$\mathbf{y} = \begin{pmatrix} \sum_i g_{x_i}^2 x_i + \sum_i g_{x_i} g_{y_i} y_i + \sum_i g_{x_i} g_{z_i} z_i \\ \sum_i g_{x_i} g_{y_i} x_i + \sum_i g_{y_i}^2 y_i + \sum_i g_{y_i} g_{z_i} z_i \\ \sum_i g_{x_i} g_{z_i} x_i + \sum_i g_{y_i} g_{z_i} y_i + \sum_i g_{z_i}^2 z_i \end{pmatrix}.$$

5. DETECTION OF 3D POINT LANDMARKS

The 3D edge intersection approach requires the detection of point landmarks. Recently, 3D differential operators for point landmark detection have been introduced[3] which are 3D extensions of existing 2D corner detectors.[7,8,11,10] The operators only employ first-order partial derivatives and therefore do not suffer from potential instabilities of high-order partial derivatives. By contrast, other approaches employ partial derivatives of up to order three.[1,4] The 3D operators essentially exploit the matrix $\mathbf{N}$ in (4) and read $Op3(\mathbf{x}) = det(\mathbf{N})/tr(\mathbf{N})$, $Op3'(\mathbf{x}) = tr(\mathbf{N}^{-1})$, as well as $Op4(\mathbf{x}) = det(\mathbf{N})$. The operators have been tested for 3D MR and CT images of the human head and have yielded promising results. In fact, the operators can also be related to the localization uncertainty of the position estimate resulting from the 3D edge intersection approach. The localization uncertainty is given through the covariance matrix $\mathbf{\Sigma} = \sigma_\varepsilon^2 \mathbf{N}^{-1}$ supposed the residuals ε_i are independently and normally distributed with zero mean and variance σ_ε^2. Hence, the responses of the differential operators can also be understood as scalar measures for the localization (un-)certainty of the position estimate resulting from the 3D edge intersection approach.

6. MULTI-STEP PROCEDURES FOR 3D POINT LANDMARK LOCALIZATION

In this section, we propose three multi-step procedures for 3D point landmark localization. We combine the 3D differential operators for landmark detection with the 3D edge intersection approach for refined localization.

i) Two-step procedure
First, points are detected with either $Op3$, $Op3'$, or $Op4$ (see Section 5), where a large operator size is chosen for reasons of robustness w.r.t. noise in images. Second, to refine the positions, a small operator size is chosen and the respective differential operator is applied within a small neighborhood around the detected points. A similar procedure for 2D point landmark localization was proposed earlier.[12,11]

ii) Two-step procedure with subvoxel localization
First, points are detected with either $Op3$, $Op3'$, or $Op4$. Second, the positions are refined through the 3D edge intersection approach (see Section 4). This scheme essentially is the 3D extension of the two-step procedure of Förstner and Gülch.[5]

iii) Three-step procedure with subvoxel localization
This procedure is a combination of the procedures i) and ii) and is therefore a three-step procedure. The first two steps correspond to the two-step procedure i). In the third step, the position estimates resulting from i) are further refined through the 3D edge intersection approach.

7. EXPERIMENTAL RESULTS FOR 3D SYNTHETIC DATA

We have tested the multi-step procedures for noise-free 3D synthetic images of tetrahedrons and ellipsoids. The partial derivatives of the image have been estimated with 3D extensions of the 2D filters of Beaudet.[13] For the detection step we have used a filter size of $5 \times 5 \times 5$ voxels. For the refinement steps of the procedures i) and iii) filters of size $3 \times 3 \times 3$ have been used. The components of the matrix $\mathbf{N}$ and the vector $\mathbf{y}$ in (4) are the averaged values of the partial derivatives within an observation window of width w. We have investigated various widths starting with $w = 3$. The size of the observation window for the 3D edge intersection approach has been the same as that for the detection operator. Maxima of the operator responses have been determined by a local maximum search in neighborhoods of $3 \times 3 \times 3$ voxels. In the case of several local maxima within the image, we have taken the point with the largest operator response.

Tetrahedron We define a binary tetrahedron (see Fig. 3a) through

$$T(\mathbf{x}, \beta) = \begin{cases} 1 & \text{if } x \geq 0 \ \wedge \ 0 \leq z \leq xs \ \wedge \ |y| \leq xt - z\frac{1-t^2}{2}, \\ 0 & \text{otherwise,} \end{cases}$$

where $s = \tan\beta$ and $t = \tan(\beta/2)$ and $0° \leq \beta < 90°$. This structure is a 3D generalization of an L-corner within the xy-plane (see Fig. 1a). For the construction of the 3D object the symmetric axis of the L-corner has been spread into the direction of the z-axis enclosing also the angle β with the x-axis. The shape of the tetrahedron is determined by the aperture angle β. For example, the choice $\beta = 90°$ gives the corner of a cube. In Fig. 3b, the Euclidean distances e from the localized positions to the position of the tip are depicted in dependence on the width w of the observation window for a tetrahedron with $\beta = 90°$. DET denotes the detection operator $Op3$. We see that procedure i) is only for $w = 5$ better than DET. The position estimates resulting from the procedures ii) and iii) are always significantly more accurate than those resulting from DET and i). The accuracy gets worse for DET and i) if w increases. By contrast, the accuracy for ii) and iii) gets better if w increases. This is what we expect due to our 2D study for the L-corner (see Section 3). In Fig. 3c, the localization errors for a more tapered tetrahedron with $\beta = 45°$ are shown. Obviously, the position estimates resulting from ii) and iii) are significantly more accurate than those resulting from DET and i). However, for ii) and iii) and larger observation windows the error slightly increases. We suspect that discretization errors give rise to this effect.

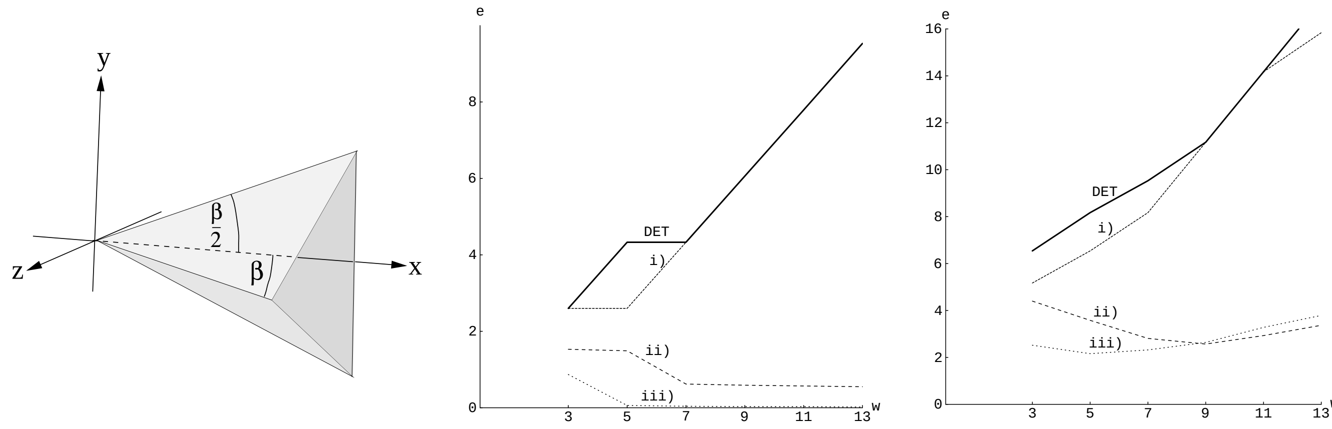

a. b. c.

Figure 3a. Tetrahedron with aperture angle β. **b and c.** Localization accuracy for tetrahedrons with $\beta = 90°$ and $\beta = 45°$, respectively. The Euclidean distances e from the localized positions to the position of the tip (ordinate) are depicted in dependence on the width w of the observation window (abscissa).

Ellipsoid A binary ellipsoid can be defined through

$$E(\mathbf{x}, a, b, c) = \begin{cases} 1 & \text{if } \frac{x^2}{a^2} + \frac{y^2}{b^2} + \frac{z^2}{c^2} \leq 1, \\ 0 & \text{otherwise,} \end{cases}$$

where a, b, and c are the lengths of the half-axes in x-, y-, and z-direction, respectively. We consider as point landmark the tip at $(0, 0, c)$. The Euclidean distances e from the localized positions to the position of the tip are depicted in dependence on the width w of the observation window for a rotationally symmetric ellipsoid w.r.t. the z-axis with $a = 8, b = 8, c = 40$ in Fig. 4a and for an ellipsoid with $a = 16, b = 8, c = 40$ in Fig. 4b. It can be seen that for the first ellipsoid the position estimates resulting from DET can be improved with procedure i). However, for the second ellipsoid the localization error for i) partly is higher in comparison to DET. The position estimates resulting from the procedures ii) and iii) generally are significantly more accurate than those resulting from DET and i). Procedure ii) improves the accuracy w.r.t. DET for about 2-3vox (vox denotes spatial unity). Procedure iii) yields for the first ellipsoid comparable results as ii). For the second ellipsoid the position estimates resulting from iii) generally are worser than those resulting from ii). In general, for DET and i) the localization error increases if the width w of the observation window increases. We also note for ii) and iii) a larger localization error for small and large values of w. For small values of w too little information for the 3D edge intersection approach is incorporated and for large values of w the approximation of the surfaces through tangent planes gets worse.

8. EXPERIMENTAL RESULTS FOR 3D MR IMAGES OF THE HUMAN HEAD

We consider as point landmarks the tips of the frontal, occipital, and temporal horns of the ventricular system, abbreviated with MC6, MC7 and MC13, respectively. The tips are indicated in Fig. 5a through black dots within

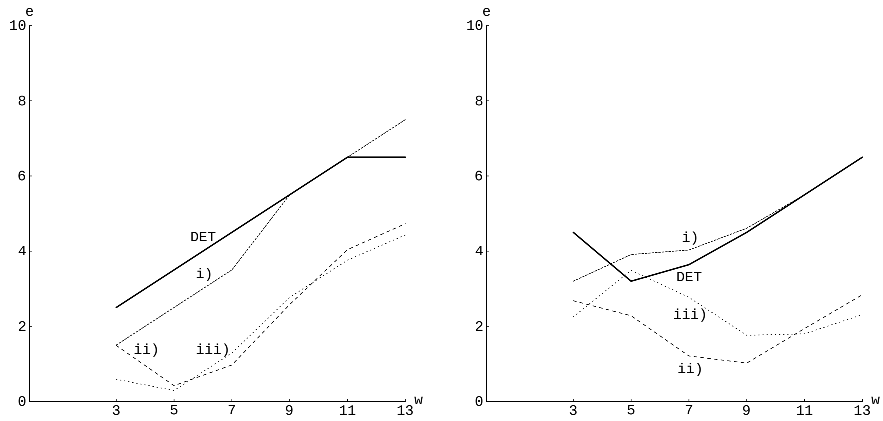

a. **b.**

Figure 4a and b. Localization accuracy for ellipsoids with half-axes lengths $a = 8, b = 8, c = 40$ and $a = 16, b = 8, c = 40$, respectively. The Euclidean distances e from the localized positions to the position of the tip at $(0, 0, c)$ (ordinate) are depicted in dependence on the width w of the observation window (abscissa).

dashed circles. The letters 'l' and 'r' denote the respective hemispheric part. In Fig. 5b, axial slices of a MR image with the horns of the ventricular system are shown. We here report on experiments for these landmarks in three

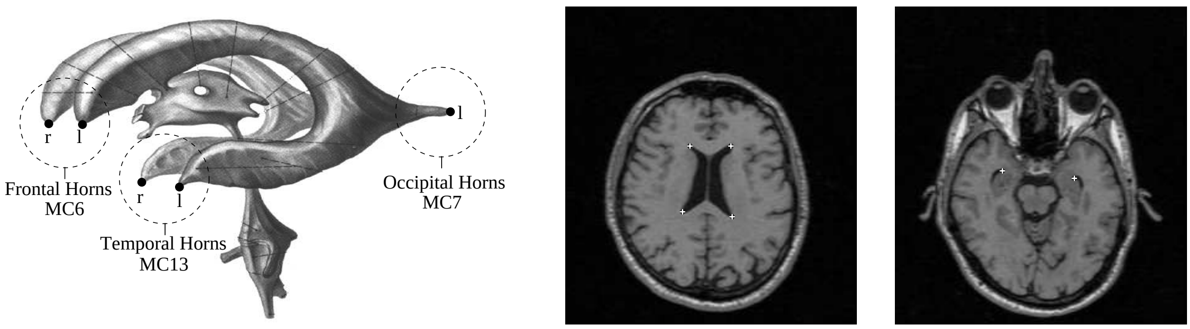

a. **b.**

Figure 5a. Anatomical preparate of the ventricular system.[14] **b.** Axial slices of a MR image with the horns of the ventriclular system. The tips of the frontal and occipital horns (left) and the tips of the temporal horns (right) in the depicted slices are marked through white crosses.

MR images. Image 1 consists of 235 sagittal slices of 256×256 voxels (voxel resolution is $1 \times 1 \times 1\text{mm}^3$), image 2 consists of 192 axial slices of 150×200 voxels (voxel resolution is $1.075 \times 1.075 \times 1.075\text{mm}^3$), and image 3 consists of 120 axial slices of 256×256 voxels (voxel resolution is $0.86 \times 0.86 \times 1.2\text{mm}^3$). We have manually specified the positions of the ventricle landmarks in the images and have taken them as 'ground truth' positions, although we are aware of the fact that manual localization of 3D landmarks generally is difficult and may be prone to error. Note that we have only determined voxel positions while the multi-step procedures ii) and iii) use the 3D edge intersection approach and hence yield subvoxel positions. To extract landmark candidates, we have chosen a region-of-interest (ROI) around the 'ground truth' positions. The size of the ROI has been set to $21 \times 21 \times 21$ voxels. We have used the same filter widths to estimate the partial derivatives as in the experiments for the 3D synthetic images. The size of the observation window for the 3D edge intersection approach has been the same as that for the detection operator. To alleviate subjectivity, we have not used any thresholds on the detection operator responses. In the case of several detected points within the ROI, the selection criterion has been the detection operator response. The thus selected candidates have been visually inspected for validity, according to the semi-automatic procedure described in Section 1. Note, however, that some landmarks have required special attention.

In Tabs. 1–3, the localization results for the ventricle landmarks are shown. The first column gives the considered landmark (LM) and the used width w of the observation window for the detection operator and the 3D edge intersection approach. Then follow the respectively localized positions resulting from the detection operator alone (DET) and the procedures i), ii), and iii). All positions are relative w.r.t. the manually specified landmark positions (top row of a box). The values below are the Euclidean distances to the manually specified landmark positions. It can be seen that, in general, the procedures ii) and iii) yield the most accurate positions. Also, procedure i) generally yields better positions than DET, although not as good as ii) and iii) do. The visual inspection of the detected candidates for the left and right temporal horns MC13l,r in image 2 and the left temporal horn in image 3 has been very difficult since in these images the temporal horns are poorly pronounced. Therefore, also the positions of these landmarks resulting from manual localization are rather uncertain. All detected points for MC13l,r in image 2 and MC13l in image 3 have extremely low operator responses indicating high localization uncertainties. Therefore, the respective entries in the tables have been labeled by a question-mark '?' meaning that for these images the respective landmarks have not been considered. For the right temporal horn MC13r in image 3 two points with extremely high operator responses have been detected. Visual inspection has revealed that the respective candidates with the highest operator responses are false detections and has caused us instead to select the candidates with the second-highest operator responses. To mark the different selection criteria in this case, the corresponding entries in Tab. 3 have been labeled by an asterisk '$*$'. For the left occipital horn MC7l in image 1 and the observation window width $w = 3$ we note a relatively large localization error. Visual inspection has actually revealed a double horn which leads to two candidates with extremely high operator responses. For $w = 3$ the candidate with the highest operator response has been farer away from the manually specified position.

LM/w	DET	i)	ii)	iii)
MC6l/3	1, 2, 0 2.24	0, 1, 0 1.00	0.08, 1.50, 0.85 1.73	0.79, 0.27, 0.36 0.91
MC6l/5	1, 2, 0 2.24	1, 1, 0 1.41	0.91, 0.43, 1.16 1.54	0.91, 0.59, 1.00 1.47
MC7l/3	4, 5, 1 6.48	3, 6, 1 6.78	2.52, 6.19, 1.12 6.78	0.82, 7.46, 0.48 7.52
MC7l/5	3, 2, 2 4.12	2, 1, 1 2.45	0.53, 0.96, 1.51 1.86	0.52, 0.15, 0.86 1.02
MC13l/3	1, 2, 0 2.24	1, 1, 1 1.73	0.79, 1.88, 0.86 2.21	0.56, 0.06, 3.31 3.36
MC13l/5	2, 2, 1 3.00	2, 2, 1 3.00	0.92, 1.21, 0.88 1.76	0.59, 0.95, 0.55 1.25

LM/w	DET	i)	ii)	iii)
MC6r/3	1, 2, 0 2.24	1, 1, 0 1.41	0.03, 1.50, 0.13 1.51	0.30, 0.21, 0.52 0.63
MC6r/5	1, 2, 0 2.24	1, 2, 0 2.24	0.84, 0.90, 0.76 1.45	1.44, 0.23, 1.27 1.93
MC7r/3	3, 2, 0 3.61	2, 1, 0 2.24	1.80, 1.58, 0.14 2.40	0.62, 0.52, 0.15 0.82
MC7r/5	3, 2, 0 3.61	3, 2, 0 3.61	0.75, 0.61, 0.82 1.27	0.28, 0.03, 0.89 0.93
MC13r/3	0, 1, 2 2.24	0, 1, 1 1.41	0.91, 0.41, 0.87 1.33	0.72, 0.61, 1.31 1.61
MC13r/5	1, 1, 5 5.20	1, 1, 4 4.24	0.60, 0.30, 5.67 5.71	1.51, 0.75, 2.68 3.17

Table 1. Localized positions of the ventricle landmarks in MR image 1 (see text).

LM/w	DET	i)	ii)	iii)
MC6l/3	2, 2, 0 2.83	2, 2, 0 2.83	1.61, 1.16, 1.04 2.24	1.58, 1.18, 1.74 2.63
MC6l/5	2, 2, 1 3.00	2, 2, 0 2.83	1.03, 0.17, 1.25 1.63	1.39, 0.23, 2.78 3.12
MC7l/3	0, 4, 1 4.12	0, 3, 0 3.00	0.10, 3.20, 0.08 3.21	0.05, 2.49, 0.97 2.67
MC7l/5	0, 4, 1 4.12	0, 4, 1 4.12	0.45, 1.81, 0.46 1.92	0.31, 1.00, 0.55 1.18
$^{?}$MC13l/3	2, 1, 2 3.00	2, 2, 1 3.00	2.20, 1.38, 2.71 3.76	2.52, 4.47, 1.84 5.45
$^{?}$MC13l/5	2, 1, 2 3.00	2, 1, 2 3.00	1.86, 1.86, 3.49 4.37	1.62, 2.66, 2.96 4.30

LM/w	DET	i)	ii)	iii)
MC6r/3	1, 2, 2 3.00	1, 2, 1 2.45	0.43, 0.88, 1.87 2.11	0.39, 0.92, 0.24 1.03
MC6r/5	1, 2, 2 3.00	1, 2, 2 3.00	0.24, 0.26, 1.64 1.68	0.71, 0.28, 1.59 1.76
MC7r/3	1, 5, 3 5.92	1, 4, 2 4.58	0.50, 3.06, 1.77 3.57	0.04, 1.07, 0.05 1.07
MC7r/5	2, 6, 4 7.48	1, 5, 3 5.92	1.39, 1.08, 1.22 2.14	0.09, 0.53, 0.42 0.68
$^{?}$MC13r/3	6, 3, 2 7.00	6, 3, 1 6.78	6.22, 3.00, 1.63 7.10	5.82, 3.00, 1.08 6.64
$^{?}$MC13r/5	6, 3, 1 6.78	5, 3, 1 5.92	6.50, 3.16, 0.87 7.28	5.94, 2.67, 1.09 6.60

Table 2. Localized positions of the ventricle landmarks in MR image 2 (see text).

In Figs. 6a and 6b, the mean values $\overline{e}$ for both $w = 3$ and $w = 5$ of the Euclidean distances from the localized positions to the manually specified positions are depicted according to each landmark and according to each MR image, respectively. The landmarks which are labeled by a question-mark in Tabs. 2 and 3 have not been taken into account for the computation of the mean values. The graphs exhibit the superior localization capabilities of ii) and iii) in comparison to i) and the detection operator alone. All in all, for DET the mean of the Euclidean distances from the

LM/w	DET	i)	ii)	iii)
MC6l/3	1, 2, 0 2.24	0, 1, 0 1.00	0.52, 0.90, 0.64 1.23	0.59, 0.17, 0.06 0.62
MC6l/5	1, 2, 0 2.24	1, 2, 0 2.24	0.07, 0.14, 1.71 1.72	0.27, 0.57, 1.58 1.70
MC7l/3	2, 3, 1 3.74	1, 2, 0 2.24	1.09, 0.39, 0.77 1.39	0.14, 0.12, 0.75 0.77
MC7l/5	2, 3, 1 3.74	2, 2, 1 3.00	0.03, 1.76, 0.37 1.80	0.03, 1.85, 0.22 1.86
$^?$MC13l/3	2, 5, 2 5.74	3, 6, 2 7.00	2.41, 2.16, 1.75 3.68	2.98, 3.75, 1.29 4.96
$^?$MC13l/5	6, 6, 6 10.39	7, 6, 7 11.58	4.66, 7.63, 7.40 11.61	7.33, 6.59, 7.55 12.42

LM/w	DET	i)	ii)	iii)
MC6r/3	0, 2, 1 2.24	0, 1, 1 1.41	0.55, 1.13, 1.34 1.84	0.53, 0.09, 1.24 1.35
MC6r/5	0, 2, 0 2.00	0, 2, 1 2.24	0.80, 0.12, 1.52 1.72	0.54, 0.02, 2.56 2.62
MC7r/3	0, 2, 0 2.00	0, 1, 0 1.00	0.30, 0.38, 0.32 0.58	0.05, 0.44, 0.52 0.69
MC7r/5	0, 2, 0 2.00	0, 2, 0 2.00	0.69, 1.42, 0.42 1.63	0.44, 1.67, 0.88 1.94
*MC13r/3	1, 2, 1 2.45	0, 1, 1 1.41	2.33, 0.87, 0.29 2.50	0.31, 0.33, 0.52 0.69
*MC13r/5	0, 2, 1 2.24	0, 2, 1 2.24	1.14, 0.39, 0.14 1.21	1.27, 0, 0.27 1.30

Table 3. Localized positions of the ventricle landmarks in MR image 3 (see text).

localized positions to the manually specified positions amounts to $3.27vox$ (vox denotes spatial unity). The two-step procedure i) improves the accuracy w.r.t. DET for $0.59vox$. Additionally using the 3D edge intersection approach further improves the accuracy w.r.t. i) for $0.93vox$. Thus, the three-step procedure iii) improves the accuracy w.r.t. DET for $1.52vox$. The two-step procedure ii) improves the accuracy w.r.t. DET for $1.14vox$.

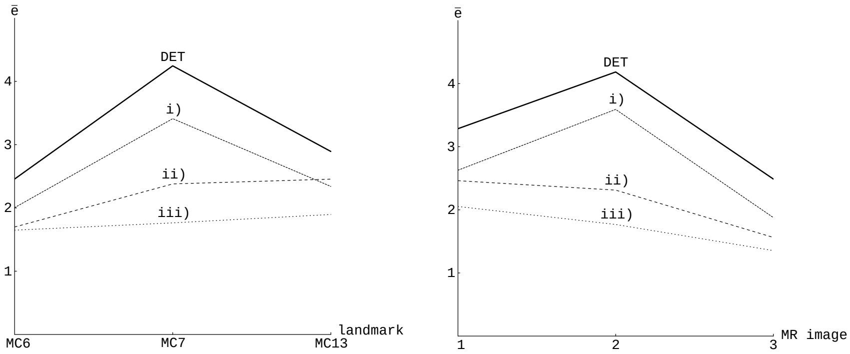

a. **b.**

Figure 6a and b. Localization accuracy of DET, i), ii), and iii) for the ventricle landmarks in the investigated MR images. The mean values $\overline{e}$ for both $w = 3$ and $w = 5$ of the Euclidean distances from the localized positions to the manually specified positions are depicted according to each landmark (a) and according to each MR image (b).

To give a visual impression of the localization capabilities of the different procedures, we also show in Fig. 7b orthogonal image cuts at the respectively localized positions for the tip of the left occipital horn in image 1 ($w = 5$). The location of the landmark within the human head is marked through a white cross in a sagittal view in Fig. 7a. Note that, due to technical reasons, the subvoxel coordinates resulting from ii) and iii) have been rounded to voxel coordinates. Nevertheless, it can be seen that the procedures ii) and iii) yield the best results.

9. CONCLUSION

We have investigated multi-step differential procedures for the detection and refined localization of 3D point landmarks. The promising results due to our theoretical investigation of the 2D edge intersection approach[5] have motivated a generalization to 3D. Based on the 3D extension of this approach, we have proposed two two-step procedures as well as one three-step procedure for subvoxel point landmark localization. These procedures combine landmark detection by applying a 3D differential operator with refined localization through the 3D edge intersection approach. We have experimentally tested these procedures for 3D synthetic images and 3D MR images of the human head. The multi-step procedures which use the 3D edge intersection approach have yielded the most accurate position estimates.

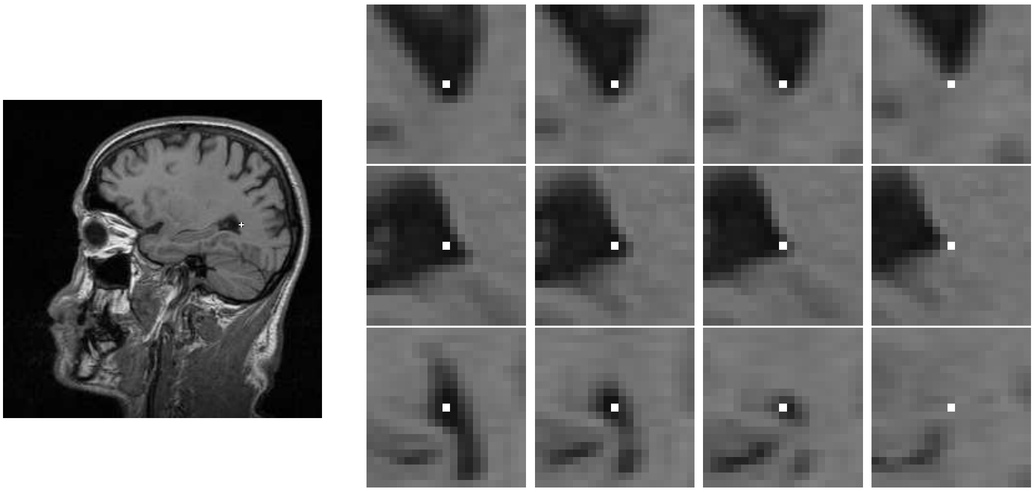

a. b.

Figure 7a. Off-sagittal slice of image 1. The manually specified position of the tip of the left occipital horn is marked through a white cross. **b.** The localized positions at the tip of the left occipital horn in image 1 ($w = 5$) are shown for DET, i), ii), and iii) (from left to right) in axial, sagittal, and coronal views (from top to bottom).

Further experiments on 3D medical images will be performed taking also other types of point landmarks into account. Future work will also concern the registration of 3D medical images using semi-automatically localized point landmarks.

ACKNOWLEDGEMENTS

Support of Philips Research Laboratories Hamburg, project IMAGINE (IMage- and Atlas-Guided Interventions in NEurosurgery), is gratefully acknowledged. The MR images have been provided by the Philips Research Laboratories Hamburg, the IMDM, University Hospital Hamburg-Eppendorf, and the AIM project COVIRA (COmputer VIsion in RAdiology).

REFERENCES

1. J.-P. Thirion, "Extremal Points: Definition and Application to 3D Image Registration," in *Proc. IEEE Conference on Computer Vision and Pattern Recognition*, pp. 587–592, (Seattle, WA, USA), 1994.
2. K. Rohr, H.S. Stiehl, R. Sprengel, W. Beil, T.M. Buzug, J. Weese, and M.H. Kuhn, "Point-Based Elastic Registration of Medical Image Data Using Approximating Thin-Plate Splines," in *Proc. Visualization in Biomedical Computing*, K.H. Höhne and R. Kikinis, eds., pp. 297–306, Springer-Verlag, (Hamburg, Germany), 1996.
3. K. Rohr, "On 3D differential operators for detecting point landmarks," *Image and Vision Computing* **15**(3), pp. 219–233, 1997.
4. W. Beil, K. Rohr, and H.S. Stiehl, "Investigation of Approaches for the Localization of Anatomical Landmarks in 3D Medical Images," in *Proc. Computer Assisted Radiology and Surgery*, H. Lemke, M. Vannier, and K. Inamura, eds., pp. 265–270, Elsevier Science, (Berlin, Germany), 1997.
5. W. Förstner and E. Gülch, "A Fast Operator for Detection and Precise Location of Distinct Points, Corners and Centres of Circular Features," in *Proc. Intercommission Conference on Fast Processing on Photogrammetric Data*, pp. 281–305, (Interlaken, Switzerland), 1987.
6. T. Hartkens, K. Rohr, and H.S. Stiehl, "Evaluierung von Differentialoperatoren zur Detektion charakteristischer Punkte in tomographischen Bildern," in *18. DAGM-Symposium Mustererkennung*, B. Jähne, P. Geißler, H. Haußecker, and F. Hering, eds., pp. 637–644, Springer-Verlag Berlin-Heidelberg, (Heidelberg, Germany), 1996.
7. W. Förstner, "A feature based algorithm for image matching," *International Archives of Photogrammetry and Remote Sensing* **26**(3), pp. 150–166, 1986.

8. J.A. Noble, "Finding corners," in *Proc. Third Alvey Vision Conference*, pp. 267–274, (Cambridge, UK), 1987.
9. K. Rohr, "Localization Properties of Direct Corner Detectors," *Journal of Mathematical Imaging and Vision* **4**(2), pp. 139–150, 1994.
10. K. Rohr, "Modelling and identification of characteristic intensity variations," *Image and Vision Computing* **10**(3), pp. 66–76, 1992.
11. K. Rohr, *Untersuchung von grauwertabhängigen Transformationen zur Ermittlung des optischen Flusses in Bildfolgen.* Diplomarbeit, Institut für Nachrichtentechnik, Universität Karlsruhe, 1987.
12. L. Dreschler, *Ermittlung markanter Punkte auf den Bildern bewegter Objekte und Berechnung einer 3D-Beschreibung auf dieser Grundlage.* Dissertation, FB Informatik, Universität Hamburg, 1981.
13. P. Beaudet, "Rotationally invariant image operators," in *Proc. International Conference on Pattern Recognition*, pp. 579–583, (Kyoto, Japan), 1978.
14. J. Sobotta, *Atlas der Anatomie des Menschen*, vol. 19, Urban & Schwarzenberg, München, Germany, 1988.